Unification of nonequilibrium molecular dynamics and the mode-resolved phonon Boltzmann equation for thermal transport simulations

Yue Hu,[1,*] Tianli Feng,[2,*] Xiaokun Gu [ID],[3] Zheyong Fan,[4] Xufeng Wang,[5] Mark Lundstrom,[5] Som S. Shrestha,[2] and Hua Bao [ID][1,†]

[1]*University of Michigan–Shanghai Jiao Tong University Joint Institute, Shanghai Jiao Tong University, Shanghai 200240, P. R. China*
[2]*Energy and Transportation Science Division, Oak Ridge National Laboratory, Oak Ridge, Tennessee 37831, USA*
[3]*Institute of Engineering Thermophysics, School of Mechanical Engineering, Shanghai Jiao Tong University, Shanghai 200240, China*
[4]*QTF Centre of Excellence, Department of Applied Physics, Aalto University, FI-00076 Aalto, Finland*
[5]*School of Electrical and Computer Engineering, Purdue University, West Lafayette, Indiana 47907, USA*

Nano-size confinement induces many intriguing non-Fourier heat conduction phenomena, such as nonlinear temperature gradients, temperature jumps near the contacts, and size-dependent thermal conductivity. Over the past decades, these effects have been studied and interpreted by nonequilibrium molecular dynamics (NEMD) and phonon Boltzmann transport equation (BTE) simulations separately, but no theory that unifies these two methods has ever been established. In this work, we unify these methods using a quantitative mode-level comparison and demonstrate that they are equivalent for various thermostats. We show that different thermostats result in different non-Fourier thermal transport characteristics due to the different mode-level phonon excitations inside the thermostats, which explains the different size-dependent thermal conductivities calculated using different reservoirs, even though they give the same bulk thermal conductivity. Specifically, the Langevin thermostat behaves like a thermalizing boundary in phonon BTE and provides mode-level thermal-equilibrium phonon outlets, while the Nose-Hoover chain thermostat and velocity rescaling method behave like biased reservoirs, which provide a spatially uniform heat generation and mode-level nonequilibrium phonon outlets. These findings explain why different experimental measurement methods can yield different size-dependent thermal conductivity. They also indicate that the thermal conductivity of materials can be tuned for various applications by specifically designing thermostats. The unification of NEMD and phonon BTE will largely facilitate the study of thermal transport in complex systems in the future by, e.g., replacing computationally unaffordable first-principles NEMD simulations with computationally less expensive spectral BTE simulations.

I. INTRODUCTION

Nanoscale heat transport is critical for the thermal management of electronics and thermoelectric energy harvesting [1–7]. When system sizes are comparable with or smaller than the phonon mean free path, phonons can move ballistically through the systems and induce many intriguing non-Fourier heat conduction phenomena such as nonlinear temperature gradients, temperature jumps near the contacts, and size-dependent thermal conductivity [8–11]. Therefore, nanoengineering has been used extensively to tune the thermal conductivity of nanomaterials for various applications [1,9,12].

Significant advances in understanding nanoscale heat conduction phenomena have been made in the past two decades by using the phonon Boltzmann transport equation (BTE) theory [9,13–16] and molecular dynamics (MD) simulations [14,17–19]. The phonon BTE uses the phonon gas model and explains the non-Fourier thermal transport by the size confinement of the ballistic phonons, which have mean free paths comparable with or longer than the system size. Compared with the gray phonon BTE [16], which often assumes that all phonons share the same velocity, mean free path, and specific heat, nonequilibrium MD (NEMD) simulations are more accurate because they naturally include all the mode-resolved properties and all the orders of anharmonicity. However, the use of NEMD simulations has been limited to the real-space interpretation without physical insights into the mode-resolved phonon transport for a long time [14,20–31]. Very recently, Zhou *et al.* [32] and Feng *et al.* [33] developed methods to map the real-space atomic vibration in NEMD to the reciprocal-space phonon properties, e.g., phonon heat flux and temperature, and give direct physical insights into the non-Fourier phonon transport. However, whether these phonon mode-resolved properties, e.g., mean free paths, temperature gradients, and heat fluxes, extracted from NEMD simulations are equivalent to those obtained from the BTE simulations remains a question. The equivalence of NEMD and phonon BTE simulations is of great importance to

———
*These authors contributed equally to this work
†Author to whom correspondence should be addressed: hua.bao@sjtu.edu.cn

establishing the fundamental theory of phonon transport as well as the use of one method to replace the other in certain situations. For example, if equivalence can be proven, one can run computationally less expensive BTE simulations to replace the computationally unaffordable NEMD simulations such as the large-scale or first-principles NEMD simulations. Another unanswered question is whether the reservoir-dependent thermal conductivity observed in NEMD simulations can be reproduced by phonon BTE theory. This question is critical to helping experimentalists understand the dependence of measured thermal conductivity on measurement methods, as well as the tunability of thermal conductivity by tuning thermal reservoirs.

A quantitative comparison of NEMD and phonon BTE is performed in this study using silicon as the testing material. However, there are several key differences between this comparison and those that were done previously [19,34–36]. First, the input parameters of phonon BTE (phonon specific heat, group velocity, and relaxation time) are extracted from the same interatomic potential as those used in NEMD. Second, the same method of thermal excitations (i.e., thermal reservoirs) in NEMD and phonon BTE is used. Third, nongray (mode-resolved) phonon BTE is solved with the only assumption being the relaxation time approximation, which should be valid for silicon. Last, instead of comparing thermal conductivity values, the temperature profiles, heat flux profiles, and phonon modal temperature of NEMD and BTE were compared directly.

As will be shown, a quantitative agreement between NEMD and phonon BTE can be achieved. Such agreement allows us to unify the phonon interpretation of the non-Fourier heat conduction effects in the two methods. Moreover, we clarify why different thermal reservoirs in NEMD simulations give different results, which has been a subject of debate for a long time [19,21,37,38].

This manuscript is organized as follows. In Sec. II, NEMD simulations with sufficiently large thermal reservoirs are described, and we revisit the difference among the Langevin thermostat, the Nose-Hoover chain (NHC) thermostat, and the velocity rescaling (VR) method. Especially, we study the heat flux profiles and phonon modal temperature inside sufficiently large reservoirs, which were not considered in previous work [21,33,37]. In Sec. III, we provide a quantitative comparison and a mode-to-mode correspondence between NEMD and the mode-resolved phonon BTE, from which a unified phonon interpretation of the non-Fourier heat conduction can be obtained. In Sec. IV, some important issues in the phonon interpretation are further proved by NEMD simulations. In Sec. V, we discuss the above phenomena according to the unified phonon interpretation as well as the relationship between the interpretation and experimental measurement. In Sec. VI, we give a summary and conclusions.

II. NEMD SIMULATIONS

NEMD simulations are an effective method to study nanoscale heat conduction [3–6,20,24–27,39]. The implementation of NEMD simulations is analogous to the experimental steady-state thermal conductivity measurements in which two reservoirs (one heat source and one heat sink) are added to the
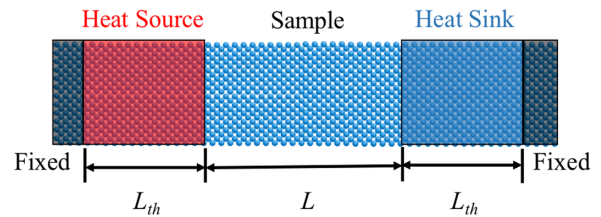

FIG. 1. Schematic illustration of the simulation cell used in NEMD simulations. The simulation cell is a piece of atomic structure. Two thermal reservoirs (one heat source and one heat sink) each with a length of L_{th} are established. The region between two thermal reservoirs is defined as the sample region with a length of L. A few layers of atoms at the two ends of the transport direction are fixed. Periodic boundary conditions are set in the directions perpendicular to the transport direction.

system to generate a one-dimensional (1D) steady-state heat transfer profile in the sample region. In NEMD simulations, one can either apply a constant heat flux by the VR method [40,41] or a temperature difference by some thermostats such as the Langevin thermostat [42] and the NHC thermostat [43–45]. By measuring the ratio of the heat flux to the temperature gradient, the thermal conductivity of the sample can be obtained according to the Fourier law. The NEMD setup is shown in Fig. 1. The reservoirs and sample lengths are L_{th} and L, respectively. To study the device size effects, $L = 13$ and 56 nm are simulated. To prevent the atoms in the thermal reservoirs from sublimating, a few layers of atoms at the two ends are fixed. Periodic boundary conditions are applied in the lateral directions.

We chose silicon modeled by the Tersoff potential [46] as the testing material throughout this work. All the NEMD simulations were performed using the large-scale atomic/molecular massively parallel simulator (LAMMPS) package [47]. The cross-sectional area is set as 8×8 unit cells, which is large enough to eliminate the finite-size effects in the lateral directions. The time step is set as 1 fs, which is short enough to resolve all the phonon frequencies. The whole system is first relaxed under the *NPT* (constant mass, pressure, and temperature) ensemble for 5 ns and then switched to the *NVE* (constant mass, volume, and energy) ensemble with the heat source and heat sink being applied. The simulations are then run for 20 ns, with the data taken within the last 10 ns being used to extract the heat transport properties, e.g., the temperature and heat flux. Although it has recently been shown that LAMMPS might incorrectly implement the heat flux formula in some cases [48,49], it is accurate for crystalline silicon [50]. The heat flux values in the sample are also close to those obtained by energy conservation [30] in our cases. The phonon modal temperatures are extracted from the NEMD simulations by using the spectral phonon temperature (SPT) method developed by Feng *et al.* [33,51] (see Appendix A for a brief explanation of the SPT method). Here the temperature of a phonon mode is defined as a convenient representation of the carrier energy density, which is equal to the energy density of a phonon mode at the Boltzmann distribution, as is commonly done for both experimental and theoretical studies, as described in the literature [52,53]. For the cases that used the SPT method, the systems are run for 40 ns under the NVE
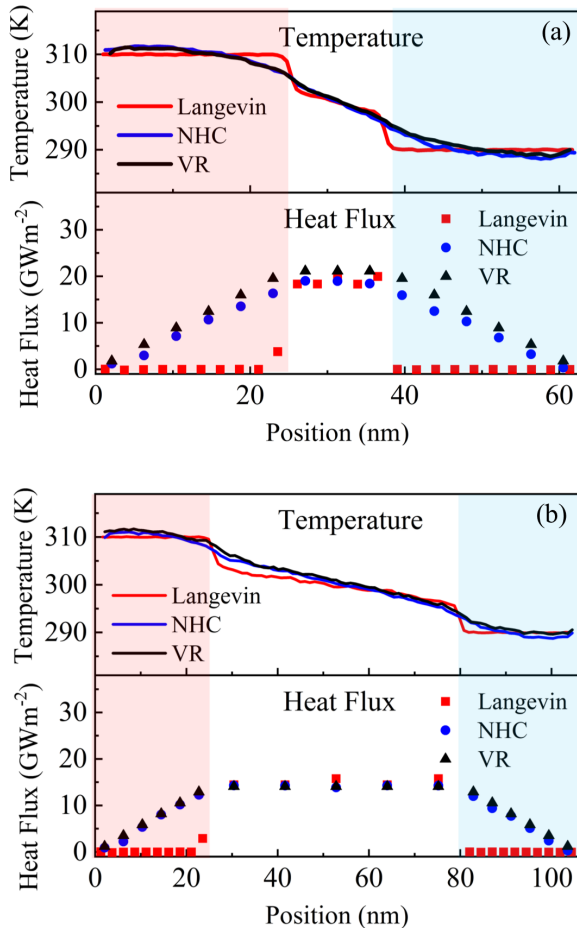
FIG. 2. Temperature and heat flux profiles for silicon with different lengths: (a) 13 nm, (b) 56 nm by using the Langevin thermostat (Langevin), the NHC thermostat, and the VR method. The shaded regions represent the heat source (red) and heat sink (blue), and the region in between represents the sample.

ensemble and the data taken within the last 20 ns are used in the SPT method.

Because thermal transport depends on thermal reservoirs, in this work, three representative thermal reservoirs, i.e., the VR method [40,41], the Langevin thermostat [42], and the NHC thermostat [43,44], are studied. The former fixes heat fluxes, and the latter two fix temperatures. The length of the thermal reservoir is first set at a relatively large value of 25 nm, and the effect of its size will be discussed later. In both the Langevin and NHC thermostats, the target temperatures of the heat source and sink are set as 310 and 290 K, respectively, with a rescaling time constant of 0.1 ps, as recommended by a previous work [37]. In the VR method, the amount of heat added for every time step depends on the size of the device: in this study, 2.50 meV is used for the 13 nm device and 1.66 meV is used for the 56 nm device.

The temperature and heat flux profiles are shown in Fig. 2. For both lengths, the temperature profiles using the Langevin thermostat are different from those of the other two thermostats. The Langevin thermostat maintains a constant temperature inside the reservoirs (except for a small region near the sample), while the other two reservoirs do not.

The Langevin thermostat produces temperature jumps at the contact regions, while the other two reservoirs do not. For all the cases, nonlinearity exists inside the sample region. The Langevin thermostat appears to give a smaller slope than the NHC thermostat and the VR method. These phenomena were also discovered in previous work [21,37].

The heat fluxes are plotted in the bottom of Figs. 2(a) and 2(b). For the Langevin thermostat, the value of the heat flux is zero inside the thermal reservoirs except for a small region near the sample. In contrast, in the NHC and VR reservoirs, the heat flux increases linearly while approaching the device. According to energy balance ($\int \dot{Q} dV = \int \mathbf{q} \cdot \mathbf{n} dA$, where $\dot{Q}$ is the volumetric heat generation rate, $\mathbf{q}$ is the heat flux and $\mathbf{n}$ is the surface normal), the heat generation rate inside the Langevin reservoirs is zero, while that inside the NHC and VR reservoirs is nearly uniform and nonzero. As such, at steady state, the Langevin thermostat only deposits heat in a small region of the reservoir near the sample and maintains a constant temperature inside the thermal reservoirs.

To further examine the temperatures of different phonon modes, the SPT method [33,51] is applied to analyze the simulation data. For simplicity, it is only applied for the case of $L = 13$ nm. We calculate the modal temperature for 204 phonon modes and plot the average value for six different phonon branches in Fig. 3.

Again, we observe distinct behavior for the Langevin thermostat, while the NHC thermostat and the VR method behave similarly. For the Langevin thermostat, the modal temperatures are out of equilibrium in the sample region but are almost at equilibrium inside the thermal reservoirs except for a small region near the sample. This phenomenon is also discovered in previous work by Feng *et al.* [33]. For the NHC thermostat and the VR method, the modal temperatures are strongly out of equilibrium not only in the sample region but also inside the thermal reservoirs.

From these results, we can distinguish the nanoscale phonon transport behaviors of different thermal reservoirs. The Langevin thermostat behaves differently, while the NHC thermostat and the VR method are similar to each other. As such, in the subsequent discussions, only the Langevin and the NHC thermostats are considered. The conclusions of the NHC thermostat should be applicable to the VR method as well.

III. PHONON BTE ANALYSIS

Based on the NEMD results from Sec. II, the NEMD simulations exhibit different behaviors with different reservoirs. In this section, we use the mode-resolved phonon BTE to model the systems studied in the NEMD simulations. The thermal excitations need to be the same in phonon BTE and NEMD. From Fig. 2, we note that for the Langevin thermostat, the temperature is uniform inside the thermal reservoir, which is similar to an infinitely large constant temperature thermal reservoir. Therefore, we consider the thermalizing boundary condition in the BTE calculations, as shown in Fig. 4(a). For the NHC thermostat, because the heat generation inside the thermal reservoir is spatially uniform, we use a uniform heat generation, as shown in Fig. 4(b). There is no heat flux in the fixed layers; thus, the fixed layers constitute an adiabatic
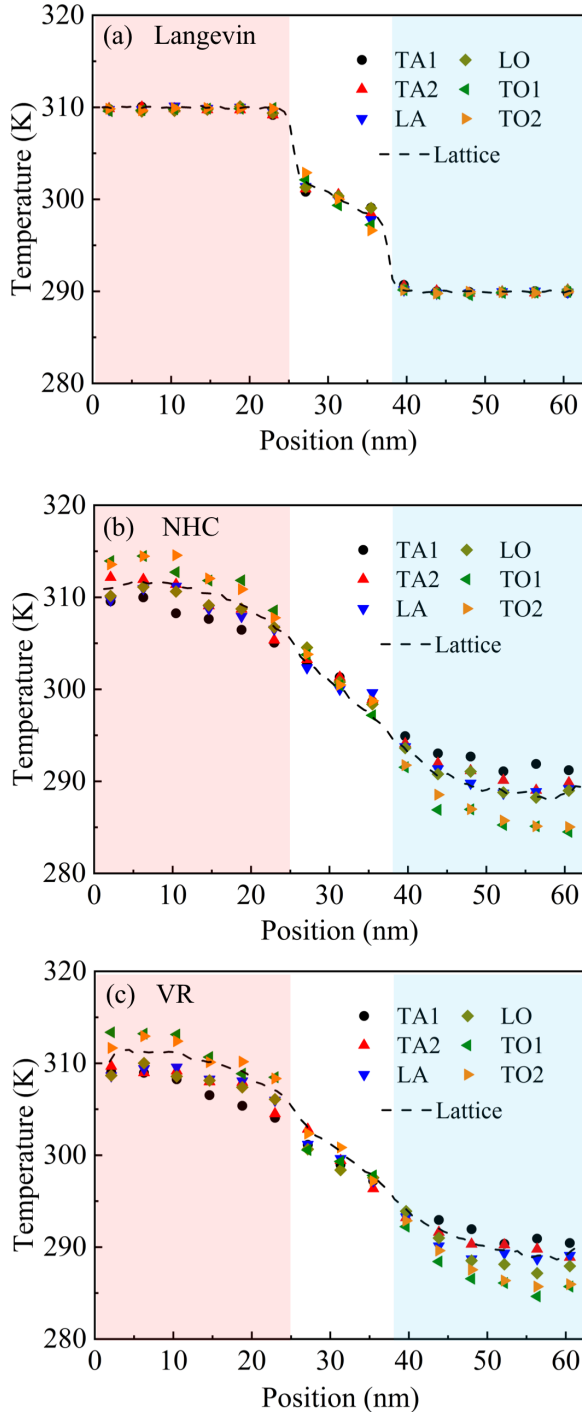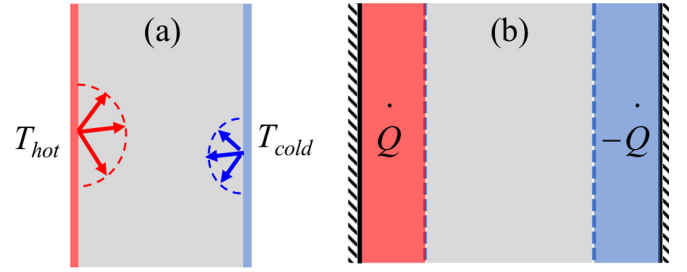
FIG. 4. The 1D simulation domain of phonon BTE with (a) thermalizing boundary condition and (b) spatially uniform heat generation and adiabatic boundary conduction.

phonons with an energy corresponding to equilibrium distribution at the target temperature into the sample region, while all incoming phonons into the surface are absorbed. For spatially uniform heat generation in Fig. 4(b), uniform thermal energy is added to the heat source and the same amount is extracted from the heat sink. Our BTE simulation is mode resolved [55], so we need to determine the amount of heat added to every phonon mode. Because it is difficult to obtain the amount of energy added to each phonon mode in the NEMD simulations, the same added energy is selected for each phonon mode. The lengths of the thermal reservoirs and the sample are set to the same as those in the NEMD simulations. Temperature is defined as the ratio of the total energy over the total heat capacity, which is consistent with that in NEMD [33,47,56]. Note that this definition is different from the lattice temperature in phonon BTE [55].

We adopted the finite volume method [10] to numerically solve the mode-resolved phonon BTE under the relaxation time approximation [57]. To solve the mode-resolved phonon BTE, the group velocity $\mathbf{v}_{\omega,p}$, the relaxation time $\tau_{\omega,p}$, and the heat capacity $C_{\omega,p}$ for every phonon mode are needed as the input information. We emphasize that the input information is extracted from the same system as NEMD: silicon crystal with Tersoff potential at 300 K. These parameters are obtained using the standard anharmonic lattice dynamics approach [58,59] in which the harmonic and anharmonic interatomic force constants are first extracted by fitting the relation between atomic forces, F, and the displacements u:

$$F_i^\alpha = -\sum_j \sum_\beta \phi_{ij}^{\alpha\beta} u_j^\beta - \frac{1}{2!} \sum_{jk} \sum_{\beta\gamma} \psi_{ijk}^{\alpha\beta\gamma} u_j^\beta \dots,$$

where (i, α) means the α direction of atom i and ϕ and ψ are the harmonic and third-order anharmonic force constants. The phonon dispersion is obtained by diagonalizing the dynamical matrix produced by the harmonic force constants. With the dispersion relation $\omega(\mathbf{q}, s)$, the group velocity and heat capacity of the mode $(\mathbf{q}, s)$ are simply calculated by $v(\mathbf{q}, s) = \partial\omega(\mathbf{q}, s)/\partial\mathbf{q}$ and $c(\mathbf{q}, s) = \partial\hbar\omega(\mathbf{q}, s)n^0(\mathbf{q}, s)/\partial T$ with the phonon population function being $n^0(\mathbf{q}, s)$. In order to make a fair comparison of the NEMD and phonon BTE results, the phonon population function used in this work has the same form as the standard Bose-Einstein distribution, $n^0(\mathbf{q}, s) = 1/(\exp(\hbar\omega(\mathbf{q}, s)/k_B T) - 1)$, but with a modified Planck's constant, which is $1/100$ of the original value [34]. This treatment could reproduce the classical distribution in MD

FIG. 3. Averaged temperature profiles for phonon modes in six different branches from NEMD simulation with (a) the Langevin thermostat, (b) the NHC thermostat, and (c) the VR method.

boundary. In the framework of phonon BTE, the adiabatic boundary can be specular or diffuse, or a mixture of both [54]. Here we briefly consider the specular boundary and will discuss this effect in detail later.

The thermalizing boundary condition in phonon BTE behaves like a black surface with the target temperature in which we set 310 K for T_{hot} and 290 K for T_{cold}, to be consistent with the NEMD simulations. This surface emits outgoing
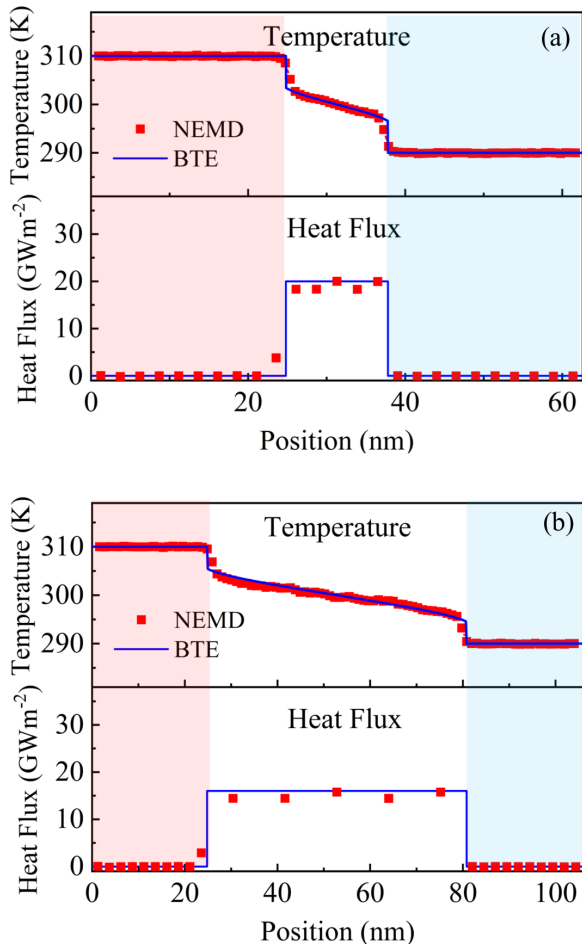
FIG. 5. Comparisons of temperature profiles and heat flux profiles between the NEMD simulations with the Langevin thermostat and the BTE calculations with the thermalizing boundary condition for two different sample lengths of (a) 13.0 nm and (b) 56.0 nm.

simulations. We compute the phonon relaxation time through the lowest-order perturbation theory, in which three-phonon processes are regarded as the only source for phonon-phonon scatterings. Computation of the three-phonon relaxation times requires the third-order anharmonic force constants, and the expression can be found in previous publications [60,61]. With these phonon properties, the thermal conductivity of silicon is calculated based on the single-mode relaxation time approximation method. We use $10 \times 10 \times 10$ q points to sample the Brillouin zone. The obtained classical thermal conductivity is 245 W/mK at 300 K, which is very close to the previous equilibrium MD result for Tersoff silicon [11]. In the BTE solver, we cannot consider as many phonon modes as are in the system due to the huge computational cost, so we use the information from 600 phonon bands obtained by averaging over the different modes. The details of averaging can be found in the previous publications [55,62].

First, we compare NEMD simulations with the Langevin thermostat and BTE simulations with a thermalizing boundary. We find that the results obtained from these two methods agree well with each other, as shown in Fig. 5, not only in the linear region in the sample but also in the nonlinear region near the reservoir. This agreement is good for various sample

lengths. The heat flux values obtained by NEMD are 19.4 and 15.4 GWm^{-2} for 13.0 and 56.0 nm, respectively. The corresponding heat flux values by BTE are 19.9 and 16.0 GWm^{-2}. The differences between the two methods are less than 5%. The differences in the temperature profiles are less than 0.5 K, which is the same magnitude as the statistical error in NEMD simulations. The apparent thermal conductivity is defined as $k = q/(\Delta T/L)$ [16,33], where q is the heat flux value inside the sample, ΔT is the average temperature difference between two reservoirs, and L is the sample length. The results are shown in Table I. Compared with the qualitative agreement obtained by the gray BTE by Dunn *et al.* [19], our mode-resolved BTE gives a quantitative agreement with NEMD results. Note that the thermal conductivity values in Table I are different from those obtained by Ref. [19] since we calculate the size-dependent thermal conductivity in different ways. In our work, we define the k as an "apparent" thermal conductivity using the temperature difference between two contacts. However, in Ref. [19], k is calculated by using the middle linear temperature region inside the device, and the obtained k has no clear physical interpretation although this method is a commonly used in NEMD simulations. As pointed out by Ref. [33], a plausible physical interpretation of using the middle linear temperature region as the temperature gradient to calculate k is that it can predict the bulk thermal conductivity if the mode-resolved heat flux and temperature are calculated and the mode-resolved thermal conductivities are summed up.

Second, we compare NEMD simulations with the NHC thermostat and BTE simulations. We find that the results are the same only when the BTE simulations use uniform heat generation reservoirs. The temperature and heat flux profiles at different sample lengths are shown in Fig. 6. The apparent thermal conductivity results also agree well, as shown in Table I. From the quantitatively good agreement between the NEMD and BTE results, we can make two important conclusions.

(1) NEMD simulations can match the mode-resolved phonon BTE quantitatively with the proper choice of thermal excitations. The Langevin thermostat is similar to a thermalizing boundary condition in BTE. The NHC thermostat with fixed layers is similar to a uniform heat generation in the thermal reservoir with adiabatic boundaries.

(2) The non-Fourier behaviors observed in NEMD simulations, including the nonlinear temperature profile, temperature jumps, and size effect, can be reproduced by the mode-resolved phonon BTE and pose a clear explanation of phonon transport.

Although the NEMD and BTE simulations are all conducted by using full phonon spectra, the comparisons discussed above are still based on an "averaged" temperature and heat flux. To further confirm our conclusions about the equivalence of NEMD and phonon BTE, we compare their mode-resolved phonon temperatures. For the case of $L = 13$ nm, temperature profiles for the six phonon branches of silicon are compared in Fig. 7. We find that the branch-resolved temperatures obtained from BTE with the thermalizing boundary condition agree well with those obtained from NEMD with the Langevin thermostat throughout the whole system, strongly supporting our conclusion about their equivalence. Regarding

TABLE I. The apparent thermal conductivity results.

Sample length (nm)	Apparent thermal conductivity (W/mK)			
	BTE with Thermalizing boundary	NEMD with Langevin reservoir	BTE with Uniform heat generation	NEMD with NHC reservoir
13.0	12.9	12.6	12.3	12.0
56.0	44.8	43.1	37.8	39.2

the comparison of NEMD with the NHC thermostat and BTE with spatially uniform heat generation, to reproduce exactly the mode-resolved temperatures inside the NHC reservoirs using BTE, careful assignment of the heat generation rate to each individual phonon mode in BTE is required, which is difficult. Here, for simplicity, we assign a uniform heat generation rate to each phonon mode, and we find that the branch-resolved temperatures obtained from the two methods share the same characteristics [Fig. 7(b)]. (1) Different branches are out-of-equilibrium inside the thermostats. (2) The phonons with shorter mean free path (TO and LO branches) become more excited in the hot reservoir and cool more in the cold reservoir, compared with the phonons with longer mean free path (TA and LA branches). These characteristics are different from the BTE with a thermalizing boundary condition or NEMD with the Langevin thermostat. By carefully assigning the heat generation rate to each individual phonon mode in the BTE reservoirs, we believe the mode-resolved phonon temperatures can match exactly those obtained from NEMD with NHC thermostat.

With the agreement between NEMD simulations and phonon BTE, we can unify the two methods based on one
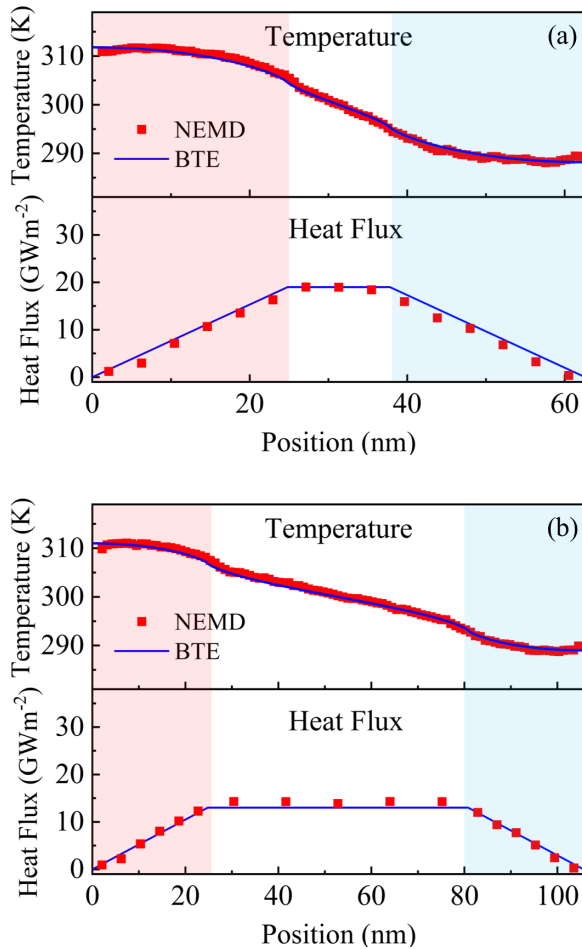

FIG. 6. Comparisons of temperature profiles and heat flux profiles between NEMD simulations with the NHC thermostat and the BTE calculations with spatially and modally uniform heat generation for two different sample lengths of (a) 13 nm and (b) 56 nm.
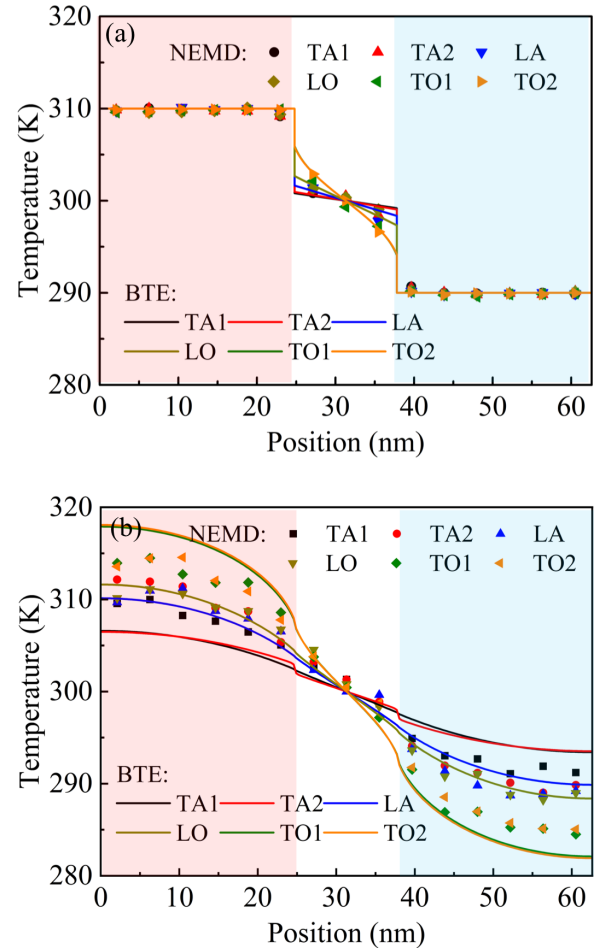

FIG. 7. (a) Comparison of temperature profiles for six different phonon branches between the NEMD simulations with the Langevin thermostat and the BTE calculations with the thermalizing boundary condition. (b) Comparison of temperature profiles for six different phonon branches between the NEMD simulations with the NHC thermostat and the BTE calculations with the uniform heat generation.
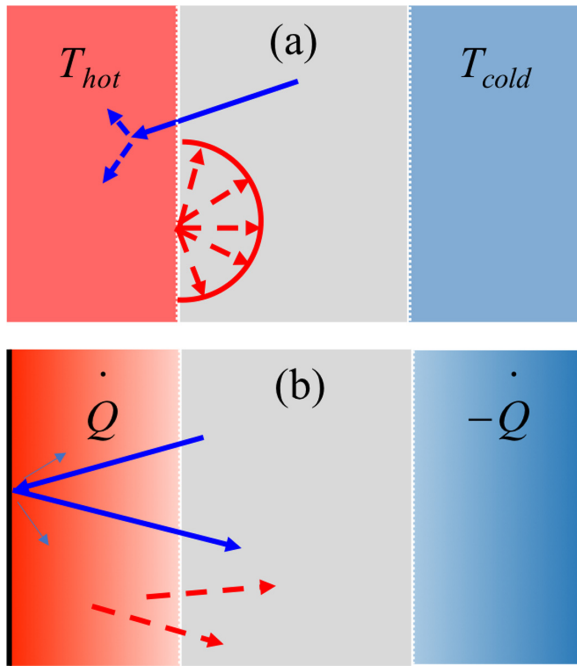
FIG. 8. Schematic illustration of the phonon interpretation of the non-Fourier heat conduction by NEMD simulations with (a) the Langevin thermostat and (b) the NHC thermostat. (a) The temperature inside thermal reservoirs remains constant (T_{hot} in the heat source and T_{cold} in the heat sink). The phonons are only emitted from the boundary of the reservoir (the small region in the reservoir near the sample region), and all have an energy density corresponding to equilibrium distribution at the same temperature. All phonons entering the boundary are absorbed. (b) Uniform heat generation occurs in the whole thermal reservoir ($\dot{Q}$ in the heat source and $-\dot{Q}$ in the heat sink). The phonons are emitted into the sample region from the whole volume and continue moving inside the entire simulation domain until they scatter with each other or the adiabatic boundary.

unified phonon interpretation of the non-Fourier heat conduction. As shown in Fig. 8(a), by using the Langevin thermostat, the thermal reservoir behaves like an infinitely large equilibrium thermal reservoir, which is similar to a thermalizing boundary condition in phonon BTE. The phonons are only emitted from the boundary of the reservoir, a small region in the reservoir near the sample, with the same temperature. Here the "phonon temperature" is a representation of the phonon energy density, with the population following the Boltzmann distribution [33]. All phonons entering through the boundary to the reservoirs are absorbed. In contrast, as shown in Fig. 8(b), the NHC thermostat or VR method in NEMD simulations excite phonons by generating uniform heat to all phonon modes throughout the whole reservoirs, which corresponds to the uniform heat generation in the phonon BTE. The phonons with shorter mean free path (TO and LO) have more scattering inside the reservoirs, and therefore, they are more easily heated in the hot reservoir and cooled in the cold reservoir, compared with other phonons with smaller scattering rates (TA and LA). This explains why the TO and LO show higher temperatures in the hot reservoir and lower temperatures in the cold reservoir, compared with TA and LA phonons, using the NHC or VR thermostat. In this case, the

heat-nonconductive phonons (TO and LO) are excited more than the heat-conductive ones (TA and LA), reducing the overall thermal conductivity of the sample, compared with the case in which all phonons are excited equally, as seen in the Langevin thermostat. This finding explains why the size-dependent thermal conductivity obtained by the NHC thermostat is smaller than that by Langevin thermostat observed in the literature [19]. Furthermore, if we construct a reservoir that can excite the TA and LA phonons more than the TO and LO phonons, the calculated size-dependent thermal conductivity can be even higher than that by the Langevin thermostat. This principle also applies to experimentation: If the contacts excite more acoustic phonons than optical phonons, the measured thermal conductivity of the sample can be larger than its intrinsic value, and vice versa. Therefore, we can tune the thermal conductivity of nanodevices by tuning the contacts in practical applications. However, when the length of the system is long enough, much longer than the phonon mean free paths, the thermal conductivity calculated or measured by all the methods reaches the same value since all the phonons can reach equilibrium inside the sample due to the diffusive scattering. That is to say, reservoirs do not affect the measured bulk thermal conductivity value.

IV. THE EFFECTS OF THERMAL RESERVOIR SIZE AND BOUNDARY

Based on the above findings, several deductions can be made. The first one is about the length of the thermal reservoirs. For the Langevin thermostat, because only the boundary (the small region in the reservoir near the sample) affects the thermal transport, the length of the thermal reservoirs should not influence the results when it exceeds the length of the small region. For the NHC thermostat, the whole volume affects the thermal transport, so the length of the thermal reservoirs should affect the results significantly. To prove this, the temperature profiles and heat flux values in the sample region for different lengths of thermal reservoirs using the Langevin and the NHC thermostats are shown in Fig. 9. From Fig. 9(a), we see that for the Langevin thermostat, when the lengths of thermal reservoirs are longer than 0.5 nm, the length essentially does not influence the temperature profile and heat flux. Therefore, only the small region near the sample affects the simulation results. This phenomenon is consistent with the findings in previous studies in which the length of the thermal reservoirs did not influence the results when it exceeded a critical value, which depended on the time parameter of the thermostat [24,32,37]. In contrast, for the NHC thermostat in Fig. 9(b), the temperature profile and heat flux value change with the length of the thermostat. Therefore, the Langevin thermostat behaves like an infinitely large thermal reservoir while the NHC thermostat is a finite-length reservoir with uniform heat generation.

The second deduction that can be made is about boundary scattering. For the infinitely large thermal reservoir, the phonons that enter are absorbed, and there is no boundary scattering. For the finite-length reservoir with uniform heat generation, the phonons can continue moving inside the thermal reservoirs, so the boundary scattering should be important
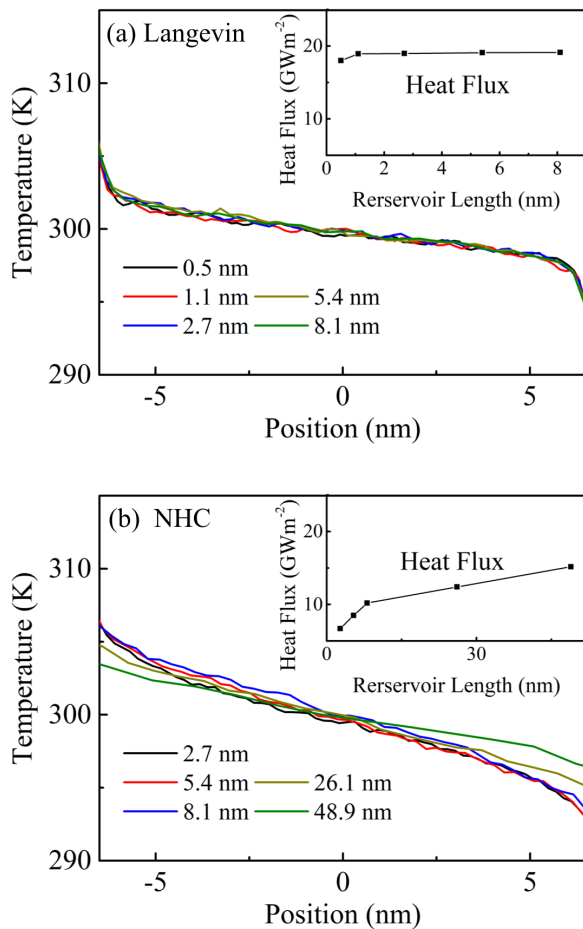
FIG. 9. Temperature profiles and heat flux values obtained by using different lengths for the thermal reservoirs: (a) the Langevin thermostat, (b) the NHC thermostat.

to the results. Thus, we set three configurations, as shown in Fig. 10, to test the boundary scattering.

In the first configuration [Fig. 10(a)], we add 2.2-nm crystal silicon between the thermal reservoirs and the fixed layers.
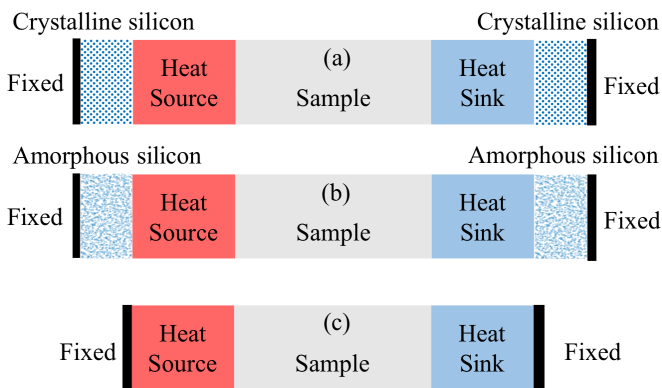

FIG. 10. Three configurations used to test boundary scattering: (a) 2.2-nm crystalline silicon was added between the thermal reservoirs and fixed layers, (b) 2.2-nm amorphous silicon was added between the thermal reservoirs and fixed layers, (c) the origin configuration used in NEMD simulation.

In the second configuration [Fig. 10(b)], we add 2.2-nm amorphous silicon between the thermal reservoirs and the fixed layers to generate diffuse phonon scattering. Recent wave packet simulations have clearly shown that a flat crystalline surface specularly scatters phonons while amorphous silicon induces strong diffuse scattering [63]. The third configuration is the same as in the previous cases [Fig. 10(c)]. We set the length of thermal reservoirs as 8.2 nm and the length of the sample as 13 nm. The temperature and heat flux profiles are shown in Fig. 11.

As shown in Fig. 11(a), the temperature profiles of these three configurations for the Langevin thermostat are very close to each other. The values of the heat flux in the sample region are also the same but are not shown here for simplicity. This result proves that the phonons entering the thermal reservoirs cannot reach the boundary when we use the Langevin thermostat. The temperature profiles of the three configurations in Fig. 11(b) are quite different for the NHC thermostat. The values of the heat flux in the sample region are also not the same, as shown in Fig. 11(c). This result proves that the phonons entering the thermal reservoirs will reach the boundary and will not be completely absorbed in the thermal reservoirs when the NHC thermostat is used. It should also be noted that the temperature drop (or increase) near the two ends is not a simulation error. The heat flux in these regions was calculated in Fig. 11(c) and proved to be zero. Because strong phonon nonequilibrium exists in these regions, the obtained temperature value is just some modal average. The drop (or increase) indicates that the modes become more in equilibrium. It does not mean there is heat flow from the heat bath to the adiabatic boundary. The origin of this phenomenon is similar to the nonlinearity of temperature and will be discussed later.

In another work by Liang *et al.*, the boundary was made into a "rough" structure to intentionally induce diffusive scattering in NEMD simulations for interface thermal resistance [38]. They also observed that boundary roughness matters for the VR method but not for the Langevin thermostat. However, they believe that the VR method is more realistic, while the Langevin thermostat generates artifacts. In fact, based on our understanding, the difference is merely due to the different natures of the VR method and the Langevin thermostat. As the VR method involves a volumetric heat generation, phonons can encounter the boundary. In comparison, the Langevin thermostat is an equilibrium thermostat in which phonons are equilibrated in the reservoir before they encounter the boundary, and thus the boundary atomic arrangement does not affect the phonon transport.

V. DISCUSSION

Based on the phonon interpretation of non-Fourier heat conduction described previously, we can unify the understandings of the non-Fourier phenomena in two methods. The nonlinearity of temperature in the sample is a physical phenomenon that is related to nondiffusive transport and local nonequilibrium of different phonon modes. In this situation, the temperature gradient not only relates to the heat flux but also to the local nonequilibrium of different phonon modes. This conclusion can be further proved by the fact that in
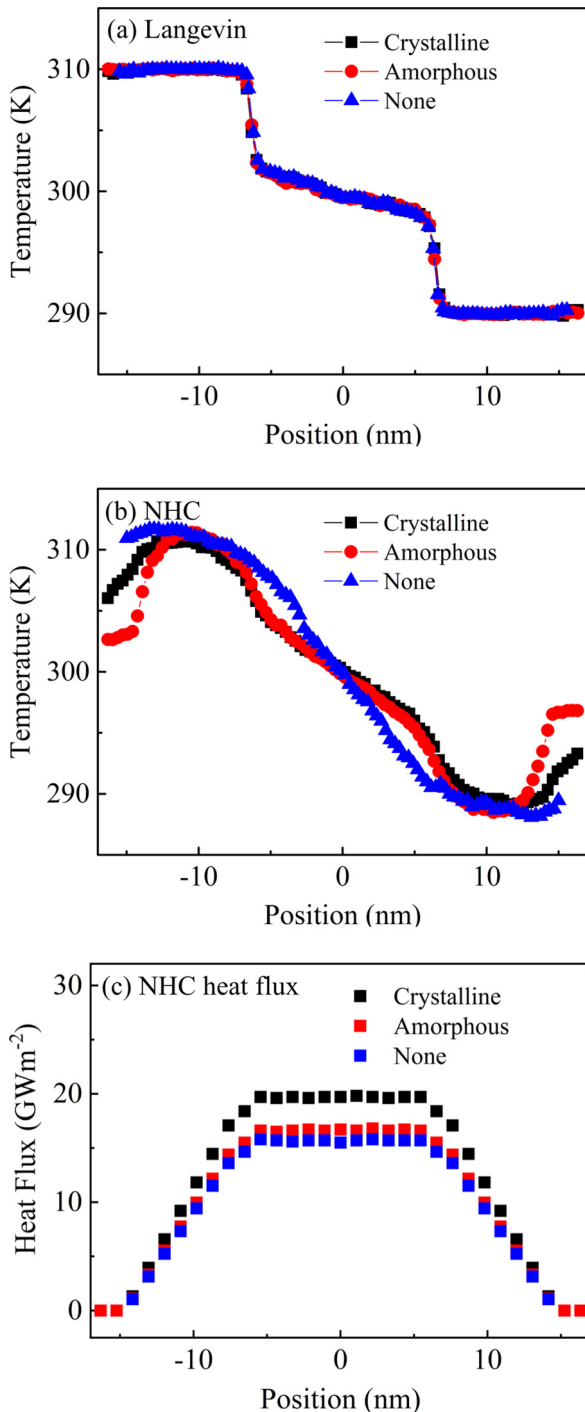
FIG. 11. Temperature profiles of (a) Langevin thermostat, (b) NHC thermostat, and (c) heat flux profiles of NHC thermostat for different simulation configurations. None, no space between fixed layers and thermal reservoirs; Crystalline, 2.2-nm crystal silicon is added between the fixed layers and thermal reservoirs; Amorphous, 2.2-nm amorphous silicon is added between the fixed layers and thermal reservoirs.

Fig. 11(b) we see a surprising phenomenon in that there is a temperature gradient near the fixed layers even though the heat flux is zero. Therefore, in Fig. 3, if the local nonequilibrium occurs in the sample for all cases, then the nonlinearity exists

for all cases, even though the heat flux is constant. The Fourier law fails in this situation because it only describes the relationship between the temperature gradient and the heat flux and ignores the effects of the local nonequilibrium. The abrupt temperature jump near the thermal reservoirs only appears when the Langevin thermostat is used. In the BTE framework, it is a normal phenomenon when a constant temperature boundary condition is applied and when ballistic transport appears [9]. Within the thermal reservoir, a fixed temperature is enforced, while in the sample region close to the thermal reservoir, the temperature is affected by the emitted phonons from the other reservoir. Some of these emitted phonons transport ballistically, and their temperature is close to the temperature of the other reservoir. This effect disappears in the diffusive regime because the phonons from the other reservoir equilibrate with other phonons during the transport process, also resulting in a continuous and linear temperature profile. In contrast, when the NHC thermostat or the VR method is used, the temperature inside the reservoirs is not enforced. Thus, the abrupt temperature jump is not obvious. The size effect is a result of ballistic transport, which agrees with our previous understanding. However, the Langevin thermostat and the NHC thermostat (or the VR method) correspond to different configurations of thermal ballistic transport, as discussed above.

The understandings developed here also help explain the results extracted from NEMD simulations. In the nondiffusive transport regime, we recommend using the Langevin thermostat to calculate the thermal conductance (or the apparent thermal conductivity) of the sample. The conductance should be obtained using $C = q/\Delta T$, where q is the heat flux value and ΔT is the temperature difference of the thermal reservoirs. The conductance obtained using the Langevin thermostat is similar to when a sample is coupled to two infinite thermal reservoirs, which has been widely adopted in the BTE [9] or Landauer framework [64]. By using this method, the results obtained from NEMD can be comparable with those of other simulation methods, including BTE, atomistic Green's function [65], and homogenous nonequilibrium molecular dynamics [66] (a method similar to equilibrium molecular dynamics) [37]. The finite-size effect of thermal conductance (or the apparent thermal conductivity) can be described by the analytical model derived by BTE [67]. Moreover, recently, Kaiser *et al.* developed a model that can obtain the same results as those of the gray phonon BTE with a thermalizing boundary condition, based on Fourier's law [16]. It is interesting to note that the key results obtained in the present work by using Langevin thermostat, the temperature profiles shown in Fig. 5, can be also approximated by following the approach of Kaiser *et al.*, which uses only the bulk thermal conductivity, specific heat, and sound velocity (see Appendix B). The accuracy is not guaranteed though, because their model does not take into account the mode-resolved phonon properties. Using the NHC thermostat or the VR method is still reasonable if the sample size is much larger than the mean free path. Nevertheless, in the nondiffusive regime, the thermal conductance obtained using either the temperature difference of the sample boundary or the temperature difference of the thermal reservoir will be dependent on the size of the reservoirs and the boundary atom arrangement. Also, because of the nonequilibrium of the

thermal reservoir, it is difficult to clearly identify the physical meaning of the obtained results. In addition, regardless of which thermal reservoir is adopted, taking the "linear region" to fit thermal conductivity should not be adopted.

Our results can also guide the measurement and control of thermal transport in real solid-state devices. We have shown that the nanoscale phonon transport characteristics, including the temperature profile, heat flux value, and modal temperature, strongly depend on the applied thermal reservoirs in NEMD simulations. This is also true for real devices. The Langevin thermostat, an infinitely large equilibrium thermal reservoir, can be realized when a dielectric film is sandwiched between two metallic films. Because the electron-phonon mean free path in the metals is much smaller than the phonon mean free path in the dielectric film, the two interfaces between the dielectric film and the metallic film can be assumed to be equilibrium thermal reservoirs at the fixed temperature [57]. The abrupt temperature jump exists in the two interfaces. The apparent thermal conductivity can be defined in the same way as that for the Langevin thermostat. In contrast, the NHC thermostat or the VR method, a uniform heat generation in the finite thermal reservoir, provides large nonequilibrium outlets. Practical heating techniques, such as optical heating or electrical heating, can result in these large nonequilibrium reservoirs, which selectively heat the optical phonon modes [68,69]. By using these techniques, the length of the thermal reservoir and the boundary conditions can significantly influence the relationship between the response and the perturbation, such as the heat flux and the temperature profile. Moreover, when comparing the experimental results in nanoscale, we must consider the correspondence of heating techniques.

VI. CONCLUSIONS

In this study, we have unified NEMD and mode-resolved phonon BTE for nanoscale thermal transport simulations using Tersoff silicon as the prototype material. By comparing NEMD and phonon BTE, we find that the thermal excitation method in the reservoirs significantly affects thermal transport in the nanomaterials. If the same thermal excitation method is used, a quantitative agreement between phonon BTE and NEMD can be achieved. Specifically, the Langevin thermostat in NEMD behaves like an infinitely large equilibrium thermal reservoir, which is similar to the thermalizing boundary condition in phonon BTE. The NHC thermostat and the VR method behave like a finite-size nonequilibrium phonon source/sink with uniform energy deposition/extraction, which can be realized by uniform generation in phonon BTE. This results in the difference in size-dependent thermal conductivity measured using different reservoirs in NEMD simulations. Because different thermal excitations are also often used in experiments with different heating techniques, our work can also explain why different experimental measurement methods produce different thermal conductivities at nanoscale. Thus, when comparing any experimental or simulation results at nanoscale, we must consider the correspondence of thermal excitations. Interpretations of all the non-Fourier behaviors in phonon BTE and NEMD are also unified due to the combi-nation of nondiffusive phonon transport and nonequilibrium among different phonon modes.

The unification of NEMD and mode-resolved BTE in this work will facilitate simulations in the future. The computationally inexpensive phonon BTE can be used to replace the computationally expensive and unaffordable NEMD simulations at large scales or by first principles. We expect our work will provide important guidance on thermal transport simulations, experimental thermal conductivity measurement, and practical heat flow manipulation.

APPENDIX A: SPT METHOD

In MD, the equilibrium phonon population is described by the Boltzmann distribution:

$$n_\lambda = \frac{k_B T_\lambda}{\hbar \omega_\lambda}. \tag{A1}$$

The total energy of the phonon mode λ at the given temperature T_λ is the per phonon energy multiplied by its population:

$$E_\lambda = n_\lambda \hbar \omega = k_B T_\lambda. \tag{A2}$$

Here, λ is short for $(\mathbf{k}, \upsilon)$, with $\mathbf{k}$ and υ representing the phonon wave vector and dispersion branch, respectively. Based on the energy equipartition theorem, the time-averaged kinetic energy $\langle E_{K,\lambda} \rangle$ and potential energy $\langle E_{V,\lambda} \rangle$ are both half of the total energy; i.e.,

$$\langle E_{K,\lambda} \rangle = \tfrac{1}{2} k_B T_\lambda. \tag{A3}$$

Based on the lattice dynamics, the kinetic energy of the mode λ is

$$E_{K,\lambda} = \tfrac{1}{2} \dot{Q}_\lambda^* \dot{Q}_\lambda, \tag{A4}$$

where $\dot{Q}_\lambda(t)$ is the time derivative of normal mode amplitude, which is given by the Fourier transform of atomic displacement in real space:

$$\dot{Q}_\lambda(t) = \frac{1}{\sqrt{N_c}} \sum_{l,b}^{N_c,n} \sqrt{m_b} \exp(-i\mathbf{k} \cdot \mathbf{r}_{l,b}) \mathbf{e}_{b,\lambda}^* \cdot \dot{\mathbf{u}}_{l,b;t}. \tag{A5}$$

l and b label the indices of the primitive cells and basis atoms with the total numbers represented by N_c and n, respectively.
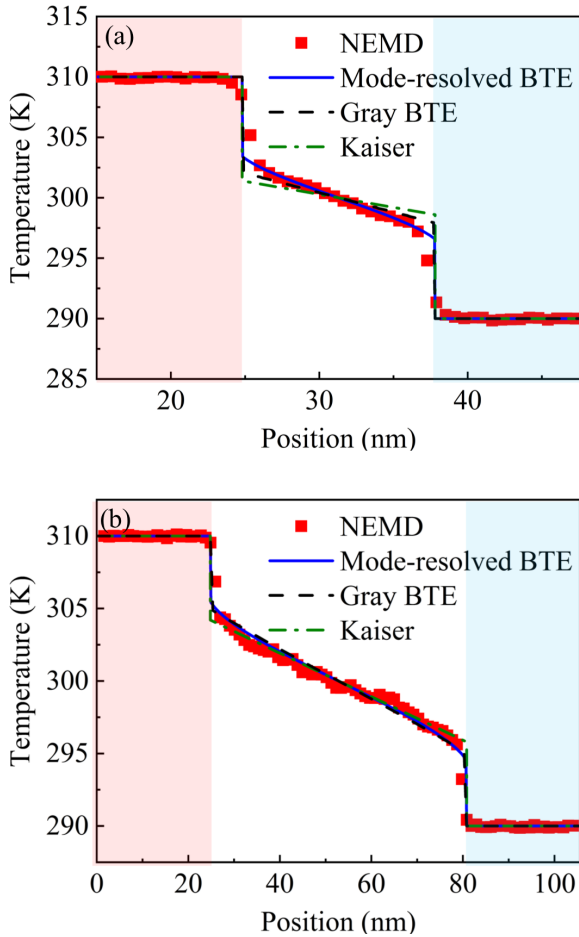
FIG. 12. Temperature profiles obtained by the NEMD simulations with the Langevin thermostat, mode-resolved BTE, gray BTE, and the approach of Kaiser et al. [16] for two different sample lengths of (a) 13.0 nm and (b) 56.0 nm.

m, $\mathbf{r}$, and $\dot{\mathbf{u}}$ are the mass, equilibrium position, and velocity vector, respectively. $\mathbf{e}^*_{b,\lambda}$ is the complex conjugate of the eigenvector component at the basis b for the mode λ. By comparing Eqs. (A4) and (A3), we can get the temperature of the phonon mode λ:

$$T_\lambda = \langle \dot{Q}^*_\lambda(t)\dot{Q}_\lambda(t)\rangle/k_B, \qquad \text{(A6)}$$

where $\langle\rangle$ denotes the time average. To eliminate the fluctuation in MD, Eq. (A6) needs to be averaged over a sufficiently long time.

APPENDIX B: APPROACH OF KAISER *et al.*

Recently, Kaiser *et al.* examined the use of the unmodified Fourier's law at the nanoscale but with temperature jump boundary conditions at the contacts of reservoirs and the sample [16]. Their results agree well with the gray phonon BTE with thermalizing boundary condition. In this section, we follow this approach to reproduce the temperature profiles and heat flux profiles in Fig. 5. In the approach of Kaiser *et al.*, the temperature profile is expressed as [16]

$$T(x) = (T_{\text{hot}} - \Delta T)\left(1 - \frac{x}{L}\right) + (T_{\text{cold}} + \Delta T)\left(\frac{x}{L}\right), \quad \text{(B1)}$$

where T_{hot} is 310 K and T_{cold} is 290 K, to be consistent with the NEMD simulations. L is the length of the sample. ΔT is the temperature jump at the contacts:

$$\Delta T = \frac{1}{2}\left(\frac{T_{\text{hot}} - T_{\text{cold}}}{1 + 3/(4Kn_x)}\right), \qquad \text{(B2)}$$

where Kn_x is the Knudsen number defined as $Kn_x = \Lambda/L$. Λ is the mean free path obtained by

$$k_{\text{bulk}} = \tfrac{1}{3}v_s\Lambda C_v. \qquad \text{(B3)}$$

The values of the bulk thermal conductivity, k_{bulk}, sound velocity, v_s, and volumetric specific heat, C_v, are all extracted from the MD simulations with classical Boltzmann distribution, which are 6000 m/s, 2.0×10^6 J/m^{3}K, and 245 W/mK, respectively. Thus, the mean free path is calculated as 59.2 nm. By using this method, we calculate the temperature profiles for the two sample lengths of 13.0 and 56.0 nm, which are shown in Fig. 12 compared with NEMD results, gray BTE results, and our mode-resolved BTE results in the main text.

Kaiser's approach is an approximate gray model solution to the phonon BTE. As shown by Kaiser *et al.* [16], as well as in Fig. 12, the solution is consistent with the gray BTE. While compared to NEMD, Kaiser's approach or the gray BTE can overestimate the thermal conductivity especially at the ballistic limit (not shown in the paper) since they use a single acoustic velocity value to represent the whole broad acoustic and optical phonon spectrum. This, again, emphasizes the significance of mode-resolved BTE.

[1] D. G. Cahill, P. V. Braun, G. Chen, D. R. Clarke, S. Fan, K. E. Goodson, P. Keblinski, W. P. King, G. D. Mahan, A. Majumdar, H. J. Maris, S. R. Phillpot, E. Pop, and L. Shi, Appl. Phys. Rev. **1**, 011305 (2014).

[2] H. Bao, J. Chen, X. K. Gu, and B. Y. Cao, ES Energy Environ. **1**, 16 (2018).

[3] X. Xu, L. F. C. Pereira, Y. Wang, J. Wu, K. Zhang, X. Zhao, S. Bae, C. Tinh Bui, R. Xie, J. T. L. Thong, B. H. Hong, K. P. Loh, D. Donadio, B. Li, and B. Özyilmaz, Nat. Commun. **5**, 3689 (2014).

[4] C. Shao, X. Yu, N. Yang, Y. Yue, and H. Bao, Nanoscale Microscale Thermophys. Eng. **21**, 201 (2017).

[5] N. Yang, T. Luo, K. Esfarjani, A. Henry, Z. Tian, J. Shiomi, Y. Chalopin, B. Li, and G. Chen, J. Comput. Theor. Nanosci. **12**, 168 (2015).

[6] T. Luo, K. Esfarjani, J. Shiomi, A. Henry, and G. Chen, J. Appl. Phys. **109**, 074321 (2011).

[7] A. Rai and A. L. Moore, Compos. Sci. Technol. **144**, 70 (2017).

[8] A. A. Joshi and A. Majumdar, J. Appl. Phys. **74**, 31 (1993).

[9] G. Chen, *Nanoscale Energy Transport and Conversion: A Parallel Treatment of Electrons, Molecules, Phonons, and Photons* (Oxford University Press, Oxford, 2005).

[10] J. Y. Murthy and S. R. Mathur, J. Heat Transfer **124**, 1176 (2002).

[11] H. Dong, Z. Fan, L. Shi, A. Harju, and T. Ala-Nissila, Phys. Rev. B **97**, 094305 (2018).

[12] D. G. Cahill, W. K. Ford, K. E. Goodson, G. D. Mahan, A. Majumdar, H. J. Maris, R. Merlin, and S. R. Phillpot, J. Appl. Phys. **93**, 793 (2003).

[13] D. Li and A. J. H. McGaughey, Nanoscale Microscale Thermophys. Eng. **19**, 166 (2015).

[14] D. P. Sellan, E. S. Landry, J. E. Turney, A. J. H. McGaughey, and C. H. Amon, Phys. Rev. B **81**, 214305 (2010).

[15] J. M. Ziman, *Electrons and Phonons: The Theory of Transport Phenomena in Solids* (Oxford University Press, Oxford, 2001).

[16] J. Kaiser, T. Feng, J. Maassen, X. Wang, X. Ruan, and M. Lundstrom, J. Appl. Phys. **121**, 044302 (2017).

[17] S. G. Volz and G. Chen, Phys. Rev. B **61**, 2651 (2000).

[18] A. J. H. McGaughey and M. Kaviany, Phys. Rev. B **69**, 094303 (2004).

[19] J. Dunn, E. Antillon, J. Maassen, M. Lundstrom, and A. Strachan, J. Appl. Phys. **120**, 225112 (2016).

[20] M. Hu, P. Keblinski, and P. K. Schelling, Phys. Rev. B **79**, 104305 (2009).

[21] J. Chen, G. Zhang, and B. Li, J. Phys. Soc. Jpn. **79**, 074604 (2010).

[22] J. C. Schön and C. Oligschleger, Phys. Rev. B **59**, 4125 (1999).

[23] C. Si, X. D. Wang, Z. Fan, Z. H. Feng, and B. Y. Cao, Int. J. Heat Mass Transf. **107**, 450 (2017).

[24] K. Sääskilahti, J. Oksanen, J. Tulkki, and S. Volz, Phys. Rev. B **90**, 134312 (2014).

[25] K. Sääskilahti, J. Oksanen, S. Volz, and J. Tulkki, Phys. Rev. B **91**, 115426 (2015).

[26] J. Liu and R. Yang, Phys. Rev. B **86**, 104307 (2012).

[27] J. Liu and R. Yang, Phys. Rev. B **81**, 174122 (2010).

[28] P. C. Howell, J. Comput. Theor. Nanosci. **8**, 2129 (2011).

[29] J. R. Lukes, D. Y. Li, X. G. Liang, and C. L. Tien, J. Heat Transfer **122**, 536 (2000).

[30] P. K. Schelling, S. R. Phillpot, and P. Keblinski, Phys. Rev. B **65**, 144306 (2002).

[31] E. S. Landry and A. J. H. McGaughey, Phys. Rev. B **80**, 165304 (2009).

[32] Y. Zhou, X. Zhang, and M. Hu, Phys. Rev. B **92**, 195204 (2015).

[33] T. Feng, W. Yao, Z. Wang, J. Shi, C. Li, B. Cao, and X. Ruan, Phys. Rev. B **95**, 195202 (2017).

[34] X. Gu, Z. Fan, H. Bao, and C. Y. Zhao, Phys. Rev. B **100**, 064306 (2019).

[35] T. Tadano, Y. Gohda, and S. Tsuneyuki, J. Phys. Condens. Matter **26**, 225402 (2014).

[36] J. E. Turney, E. S. Landry, A. J. H. McGaughey, and C. H. Amon, Phys. Rev. B **79**, 064301 (2009).

[37] Z. Li, S. Xiong, C. Sievers, Y. Hu, Z. Fan, N. Wei, H. Bao, S. Chen, D. Donadio, and T. Ala-Nissila, J. Chem. Phys. **151**, 234105 (2019).

[38] Z. Liang and P. Keblinski, Phys. Rev. B **90**, 075411 (2014).

[39] Y. Zhou and M. Hu, Phys. Rev. B **95**, 115313 (2017).

[40] P. Jund and R. Jullien, Phys. Rev. B **59**, 13707 (1999).

[41] T. Ikeshoji and B. Hafskjold, Mol. Phys. **81**, 251 (1994).

[42] A. Dhar, Adv. Phys. **57**, 457 (2008).

[43] G. J. Martyna, M. L. Klein, and M. Tuckerman, J. Chem. Phys. **97**, 2635 (1992).

[44] S. Nosé, J. Chem. Phys. **81**, 511 (1984).

[45] W. G. Hoover, Phys. Rev. A **31**, 1695 (1985).

[46] J. Tersoff, Phys. Rev. B **39**, 5566 (1989).

[47] S. Plimton, J. Comput. Phys. **117**, 1 (1995).

[48] D. Surblys, H. Matsubara, G. Kikugawa, and T. Ohara, Phys. Rev. E **99**, 051301(R) (2019).

[49] P. Boone, H. Babaei, and C. E. Wilmer, J. Chem. Theory Comput. **15**, 5579 (2019).

[50] Z. Fan, Luiz Felipe C. Pereira, H.-Q. Wang, J.-C. Zheng, D. Donadio, and A. Harju, Phys. Rev. B **92**, 094301 (2015).

[51] T. Feng, Y. Zhong, J. Shi, and X. Ruan, Phys. Rev. B **99**, 045301 (2019).

[52] J. Maassen and M. Lundstrom, J. Appl. Phys. **119**, 095102 (2016).

[53] D. Mann, E. Pop, J. Cao, Q. Wang, K. Goodson, and H. Dai, J. Phys. Chem. B **110**, 1502 (2006).

[54] M. J. Fryer and H. Struchtrup, Contin. Mech. Thermodyn. **26**, 593 (2014).

[55] S. V. J. Narumanchi, J. Y. Murthy, and C. H. Amon, J. Heat Transfer **126**, 946 (2005).

[56] D. Abarbanel and J. Maassen, J. Appl. Phys. **121**, 204305 (2017).

[57] A. Majumdar, J. Heat Transfer **115**, 7 (1993).

[58] D. A. Broido, M. Malorny, G. Birner, N. Mingo, and D. A. Stewart, Appl. Phys. Lett. **91**, 231922 (2007).

[59] Z. Tong and H. Bao, Int. J. Heat Mass Transf. **117**, 972 (2018).

[60] H. Xie, X. Gu, and H. Bao, Comput. Mater. Sci. **138**, 368 (2017).

[61] S. Li, Z. Tong, and H. Bao, J. Appl. Phys. **126**, 025111 (2019).

[62] D. Singh, J. Y. Murthy, and T. S. Fisher, J. Heat Transfer **133**, 122401 (2011).

[63] C. Shao, Q. Rong, N. Li, and H. Bao, Phys. Rev. B **98**, 155418 (2018).

[64] Y. Imry and R. Landauer, Rev. Mod. Phys. **71**, S306 (1999).

[65] N. Mingo and L. Yang, Phys. Rev. B **68**, 245406 (2004).

[66] D. J. Evans, Phys. Lett. A **91**, 457 (1982).

[67] C. Hua and A. J. Minnich, J. Appl. Phys. **117**, 175306 (2015).

[68] A. K. Vallabhaneni, D. Singh, H. Bao, J. Murthy, and X. Ruan, Phys. Rev. B **93**, 125432 (2016).

[69] A. Fan, Y. Hu, H. Wang, W. Ma, and X. Zhang, Int. J. Heat Mass Transf. **143**, 118460 (2019).